

MHD instabilities developing in a conductor exploding in the skin effect mode

V. I. Oreshkin, S. A. Chaikovsky, I. M. Datsko, N. A. Labetskaya, G. A. Mesyats, E. V. Oreshkin, N. A. Ratakhin, and D. V. Rybka

Citation: *Phys. Plasmas* **23**, 122107 (2016); doi: 10.1063/1.4971443

View online: <http://dx.doi.org/10.1063/1.4971443>

View Table of Contents: <http://aip.scitation.org/toc/php/23/12>

Published by the [American Institute of Physics](#)

Articles you may be interested in

[Spatially resolved behavior of laser-produced copper plasma along expansion direction in the presence of static uniform magnetic field](#)

Phys. Plasmas **23**, 122104 (2016); 10.1063/1.4969080

[Modelling nonlinear electrostatic oscillations in plasmas](#)

Phys. Plasmas **23**, 122103 (2016); 10.1063/1.4968520

[Suppression of diamagnetism by neutrals pressure in partially ionized, high-beta plasma](#)

Phys. Plasmas **23**, 122108 (2016); 10.1063/1.4968849

[Formation of a collisionless shock wave in a multi-component plasma](#)

Phys. Plasmas **23**, 122109 (2016); 10.1063/1.4971298

MHD instabilities developing in a conductor exploding in the skin effect mode

V. I. Oreshkin,^{1,2} S. A. Chaikovsky,^{1,3,4} I. M. Datsko,¹ N. A. Labetskaya,¹ G. A. Mesyats,³
 E. V. Oreshkin,³ N. A. Ratakhin,¹ and D. V. Rybka¹

¹*Institute of High Current Electronics, SB RAS, Tomsk, Russia*

²*Tomsk Polytechnic University, Tomsk, Russia*

³*P. N. Lebedev Physical Institute, RAS, Moscow, Russia*

⁴*Institute of Electrophysics, UB RAS, Ekaterinburg, Russia*

(Received 2 September 2016; accepted 21 November 2016; published online 6 December 2016)

The results of experiments with exploding copper conductors, performed on the MIG facility (providing currents of amplitude of about 2.5 MA and rise time of 100 ns), are analyzed. With an frame optical camera, large-scale instabilities of wavelength 0.2–0.5 mm were detected on the conductor surface. The instabilities show up as plasma “tongues” expanding with a sound velocity in the opposite direction to the magnetic field gradient. Analysis performed using a two-dimensional MHD code has shown that the structures observed in the experiments were formed most probably due to flute instabilities. The growth of flute instabilities is predetermined by the development of thermal instabilities near the conductor surface. The thermal instabilities arise behind the front of the nonlinear magnetic diffusion wave propagating through the conductor. The wavefront on its own is not subject to thermal instabilities. *Published by AIP Publishing.* [<http://dx.doi.org/10.1063/1.4971443>]

I. INTRODUCTION

Interest in the electrical explosion of conductors (EEC) caused by the skin effect is associated with a variety of applications. This is, first, the electromagnetic energy transport in the vacuum transmission lines of multiterawatt generators^{1–5} capable of producing currents of 30–50 MA with rise times of less than 100 ns. These generators are currently being developed to be used in systems of controlled thermonuclear fusion based on Z-pinch.^{6–12} With this level of currents, the electromagnetic energy density in the load region is so high that the electrode surface can explode, producing plasma and thus reducing the efficiency of electromagnetic energy transport to the Z-pinch. Another EEC research area is related to the MAGO/MTF (Magnetized Target Fusion^{9,10}) and MagLIF (Magnetized Liner Inertial Fusion^{11,12}) concepts that involve compression of initially heated deuterium-tritium mixtures by imploding metal liners. To provide stable implosions of metal liners is the main concern of the MAGO/MTF and MagLIF concepts. EEC studies are also required in R&D areas such as the production of strong magnetic fields using both imploded metal shells^{13–15} and exploded single-turn solenoids^{16,17} and the electromagnetic acceleration of bodies,^{18,19} in particular, the acceleration of metal plates in shock wave experiments (see, e.g., Refs. 20–23).

The main processes that take place during an EEC caused by the skin effect are the propagation of a shock wave and a nonlinear magnetic diffusion wave (NMDW) through the conductor and the formation of a dense low-temperature plasma at the conductor surface. Nonlinear magnetic diffusion features an abnormally high rate of electromagnetic field penetration into a conductor compared to ordinary diffusion. The diffusion rate increases due to a decrease in electrical conductivity of the metal as a result of its heating by the electric current passing through it. The

propagation velocity of the nonlinear diffusion wave is determined by the rate of shifting of the current density maximum into the conductor. Nonlinear diffusion can occur only if the magnetic field is strong enough,^{15,24} i.e., its induction is greater than

$$B_0 \approx \sqrt{\frac{8\pi}{\beta}}, \quad (1)$$

where $\beta = \frac{1}{\delta \rho c_v} \frac{\partial \delta}{\partial T}$, δ and ρ are, respectively, the resistivity and density of the conductor material at normal conditions, c_v is its specific heat at constant volume, and $\frac{\partial \delta}{\partial T}$ is the temperature derivative of its resistivity. The magnetic induction B_0 for the majority of metals is several hundreds of kilogausses, which correspond to a magnetic pressure of about 10 kbar on the conductor surface. Therefore, the nonlinear diffusion wave propagates through the conductor together with the shock wave caused by the magnetic pressure on the conductor surface.

A nonlinear magnetic diffusion wave propagating through a conductor can be accompanied by thermal instabilities, whose structure is determined by the behavior of the conductor material resistivity depending on temperature and density.^{25–27} When the resistivity increases with temperature, which is typical of the majority of metals in the liquid and solid states, the thermal instabilities give rise to layered structures (strata) with the layers arranged normal to the direction of the current flow.^{28,29} This process is intensified as the material resistivity increases with decreasing density, as with EEC. It was shown³⁰ that when an NMDW propagates through a conductor, the long-wave modes of thermal instabilities (with wavelengths of the order of the conductor thickness) are suppressed, and the short-wave modes can be unstable. However, the model³⁰ considered neither the

shock-wave nor the dissipative processes, such as heat conduction and viscous damping, which should stabilize the propagation of an NMDW. These factors can be taken into account only in a detailed magnetohydrodynamic (MHD) simulation. To perform such a simulation was an aim of the present study.

The increase in the magnetic field at the surface of a conductor to

$$B_s \approx \sqrt{8\pi\Lambda_0}, \quad (2)$$

where Λ_0 is the metal sublimation energy under normal conditions, results in the conductor explosion and in the formation of high-density, low-temperature plasma at its surface.^{31,32} For the majority of metals, B_s ranges between 2 and 4 MG.^{31,32} It is well known that magnetically confined plasma is unstable, so that magneto-Rayleigh–Taylor instabilities can develop on its surface.^{33,34}

The aim of this study was to analyze the development of instabilities arising in conductors electrically exploding in a skin effect mode at a magnetic field greater than B_s , which is typical for the EECs that occurred in the MagLIF experiments.^{11,12} A two-dimensional MHD simulation was carried out to interpret the results of experiments with copper conductors exploded at a current of about 2.5 MA within a current pulse rise time of 100 ns.

II. MIG-BASED EXPERIMENTS

The EEC experiments were performed on the MIG pulse generator,^{35–38} which is capable of producing current pulses of amplitude up to 2.5 MA and rise time of 100 ns. The MIG electric circuit comprises a line pulse transformer, water-insulated pulse-forming lines, and a load. A capacitor bank capable of storing about 400 kJ of energy is used as an energy store. The line pulse transformer with 190-nF series capacitance transfers the energy stored in the capacitor bank to the first pulse-forming line of electric length 75 ns and a characteristic impedance of 1.3 Ω . Once an uncontrolled single-channel water-insulated spark gap operates, part of the energy is transferred to the second pulse-forming line of electric length 26 ns and an impedance, 0.65 Ω , and after operation of a nine-channel water-insulated spark gap, up to 120 kJ of energy with a power of 1.2–1.4 TW is supplied, through a transmission line of characteristic impedance 0.65 Ω , to the load.

Cylindrical metal conductors of length 1–1.2 cm and varied in diameter were used for the load. Here, we present only the experimental data for copper conductors of diameter 1 mm. The conductors were mounted in the electrode gap of the MIG generator. The diagnostics included electrical measurements of current and voltage and measurements of the self-radiation of exploding conductors using vacuum X-ray diodes (XRDs). The XRDs had an open aluminum cathode and were used with no filter. The sensitivity of this type of detector peaks in the spectral range 10–15 eV and falls sharply in both the short-wave and the long-wave spectral region. Therefore, in the experiment, a signal was detected as a plasma of temperature $T \approx 2$ eV was formed at the

conductor surface. To take an image of the conductors in the visible spectrum, an HSFC Pro four-frame optical camera providing a 3-ns exposure time and 50- μ m spatial resolution was used.

Figure 1 shows the waveforms of the current pulse and the XRD signal produced by the explosion of a copper wire 1 mm in diameter, and the calculated time dependence of the brightness temperature of the surface. The solid circles mark the times at which the HSFC Pro optical camera images of the conductor (Fig. 2) were obtained. As can be seen from Fig. 1, the explosion of the conductor surface occurs within 43–45 ns (the explosion time corresponds to a sharp increase in intensity of the XRD signal and to a brightness temperature of 2 eV) from the onset of current flow at a magnetic induction of 4.2–4.5 MG, that is, when it is close to B_s (equal to 3.3 MG for copper). The magnetic induction reaches a maximum of about 8 MG within about 80 ns.

Figure 2 presents the images of a copper cylindrical conductor of diameter 1 mm taken within 70, 110, 150, and 190 ns after the onset of current flow. The image taken at the 70th ns shows no resolvable perturbation on the conductor surface. Hardly detectable transverse perturbations are observed at the 110th ns. In the third and fourth images, taken at the 150th and 190th ns, respectively, large-scale perturbations of wavelength 0.2–0.5 mm are clearly visible. Note that the instability of this type was observed in many experiments with conductors electrically exploded in a skin effect mode.^{31–33,39–43}

III. MAGNETOHYDRODYNAMIC SIMULATION OF AN EEC

To simulate the explosion process, the JULIA MHD code^{44,45} was used, which is based on the particle-in-cell method and allows one to simulate the explosion of a conductor in a two-dimensional approximation. The MHD equations used in this code are hydrodynamic equations that describe the laws of conservation of mass, momentum, and energy

$$\frac{\partial \rho}{\partial t} + \nabla \cdot (\rho \mathbf{v}) = 0, \quad (3)$$

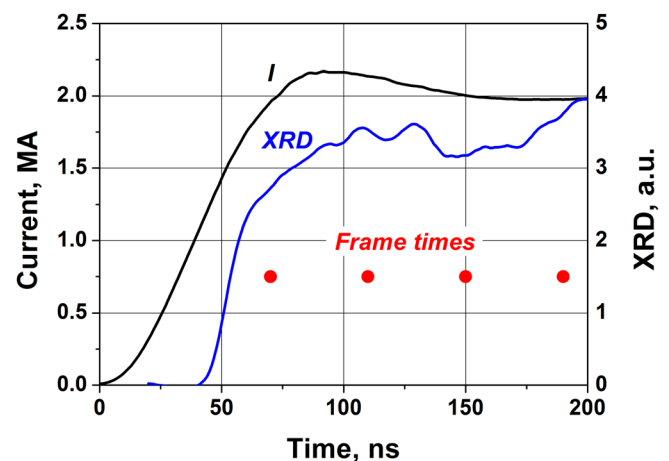


FIG. 1. Experimental time dependencies of the current through a load (copper wire of diameter 1 mm) and voltage across an XRD. The solid circles mark the time of operation of a four-frame HSFC-Pro optical camera.

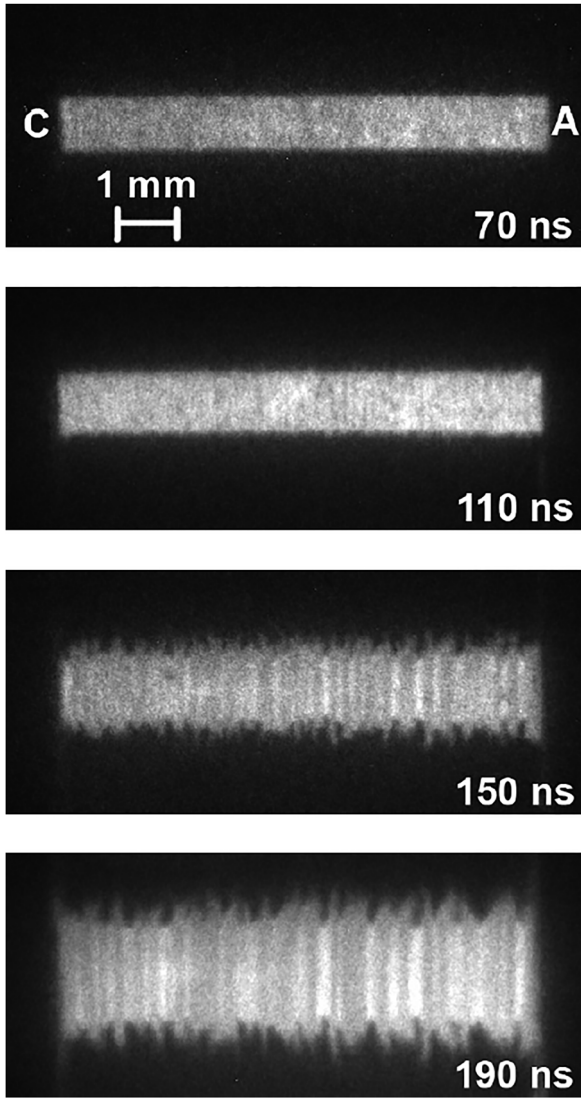


FIG. 2. Optical images taken using an HSFC-Pro camera (with a 3-ns exposure time). The camera operation times are marked by solid circles in Fig. 1.

$$\rho \frac{\partial \mathbf{v}}{\partial t} + \rho \mathbf{v} \nabla \mathbf{v} = -\nabla p + \frac{1}{c} \mathbf{j} \times \mathbf{B}, \quad (4)$$

$$\frac{\partial \rho \varepsilon}{\partial t} + \nabla(\rho \varepsilon \mathbf{v}) = -p \nabla \mathbf{v} + \frac{\mathbf{j}^2}{\sigma} + \nabla(\kappa \nabla T). \quad (5)$$

Maxwell's equations written in a quasi stationary approximation (disregarding displacement currents)

$$\frac{1}{c} \frac{\partial \mathbf{B}}{\partial t} = -\nabla \times \mathbf{E}; \quad \nabla \times \mathbf{B} = \frac{4\pi}{c} \mathbf{j}, \quad (6)$$

and Ohm's law

$$\mathbf{j} = \sigma \left(\mathbf{E} - \frac{1}{c} \mathbf{v} \times \mathbf{B} \right), \quad (7)$$

where \mathbf{v} , p , ε , and T are the velocity, pressure, internal energy, and temperature of the conductor material, respectively; \mathbf{H} is the magnetic field strength; \mathbf{E} is the electric field strength in a fixed coordinate system; \mathbf{j} is the current density; κ is the thermal conductivity; $\sigma = \delta^{-1}$ is the electric conductivity; and δ is the resistivity.

For the calculations, wide-range semiempirical equations of state⁴⁶ were used; the electrical characteristics and the thermal conductivity of the metal were calculated using conductivity tables for copper compiled using a numerical-experimental technique.^{45,47–50}

The system of equations (3)–(7) was solved in the cylindrical (r, z) geometry using the following numerical algorithm: The equation of motion (4) was solved for each particle, and then the average mass velocity and the material density were calculated by summing over all particles in each cell. The continuity equation (3) in this method is fulfilled automatically due to the Lagrangian nature of the particles. The energy balance equations (5) and Maxwell's equations (6) were solved on a fixed Eulerian grid, which was constructed at the beginning of the calculations and was not changed in the course of the numerical solution.

To solve the MHD equations, it is necessary to set boundary conditions. The boundary conditions for the equations of motion (4) can be imposed by setting either the velocity or the pressure at the boundary. When integrating Equation (4), the boundary conditions were chosen as $p=0$ at the free boundary (the boundary with vacuum). The boundary conditions at the center, at $r=0$, corresponded to the condition of axial symmetry; that is, to the radial velocity $v_r=0$. At the axial boundaries, at $z=0$ and $z=Z_{\max}$, where Z_{\max} is the maximum of the coordinate z of the Eulerian grid, $v_z=0$ was set.

The boundary conditions for the energy balance equations (5), including the heat equation, were set as the heat flux at the boundaries. Everywhere at the boundaries, the heat flux was assumed to be zero, which corresponds to the absence of external heat sources and sinks.

The boundary conditions for Maxwell's equation (6) were the following: the radial component of the electric field vector $E_r=0$ at $r=0$, $z=0$, and $z=Z_{\max}$; the azimuthal component of the magnetic field vector $B_\phi=0$ at $r=0$ and $B_\phi=2I(t)/(cR_{\max})$ at $r=R_{\max}$, where R_{\max} is the maximum radius of the Eulerian grid, and $I(t)$ is the current flowing through the conductor.

The initial conditions were chosen as 300 K for the temperature of the copper and 8.9 g/cm^3 for its average density. The computational grid was 150×150 in size, i.e., it consisted of 2.25×10^4 cells; the number of particles was 10^7 . To investigate the development of instabilities in each computational cell, a random perturbation making 1% of the average density was set. Note that the level of the initial density perturbations affects the computational results insignificantly, as at the early stage of the process, when a shock wave and a nonlinear diffusion wave propagate through the conductor, all instabilities are suppressed (see Section IV).

IV. SIMULATION RESULTS

This section presents the results of a two-dimensional MHD simulation of the electrical explosion of a copper conductor carrying a current of amplitude 2.1 MA with a rise time of less than 100 ns. The simulation used an actual experimental time dependence of the load current, which is plotted in Fig. 1. The explosion of a wire segment of length

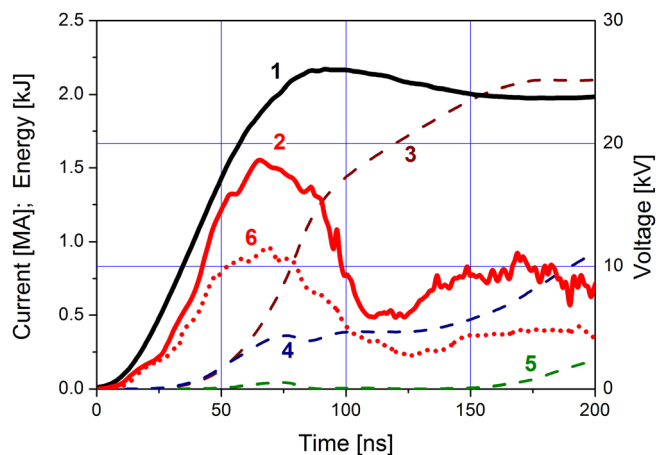


FIG. 3. Calculated time dependencies of the current through a load (curve 1), voltage across the load (curves 1 and 6), thermal energy (curve 3), magnetic energy (curve 4), and kinetic energy (curve 5). Curves 1–5 correspond to a cylindrical copper wire of diameter 1 mm and curve 6 to a planar case.

$Z_{\max} = 2.5$ mm (in the experiments, the conductor length was 1 cm) and diameter 1 mm was simulated.

Figure 3 shows the calculated waveforms of current (repeating the current waveform shown in Fig. 1) and voltage for the 1-cm long conductor, and the time behavior of

different types of energy in the conductor material: thermal ($E_{in} = 2\pi \int \int_V \epsilon r dr dz$), magnetic ($E_m = 2\pi \int \int_V \frac{B^2}{8\pi} r dr dz$), and kinetic ($E_k = 2\pi \int \int_V \frac{\rho v^2}{2} r dr dz$) (the integrals are evaluated over the volume V occupied by plasma; the conductor length is set equal to 1 cm). Figure 4 shows the spatial temperature distributions at the times corresponding to the frames obtained with an HSFC Pro optical camera that are shown in Fig. 2. Comparing the conductor images obtained in the experiment (see Fig. 2) with the calculated data (see Fig. 4), we see a good conformity between them. First, the time behavior of the diameter of the conductor plasma is the same. Second, the calculated wavelength of large-scale perturbations is in good agreement with the observations. In addition, the experimentally determined explosion time, i.e., the time at which a plasma of temperature above 2 eV is formed at the conductor surface, coincides within 10% with the calculated one. Thus, there is reason to believe that the calculation model used adequately describes the conductor explosion mode. This allows, based on the model predictions, a detailed analysis of the basic physical processes that take place during the explosion.

We first dwell on the mechanism of formation of large-scale perturbations that are visible in Fig. 2. In appearance, these perturbations resemble the strata that occur in fine

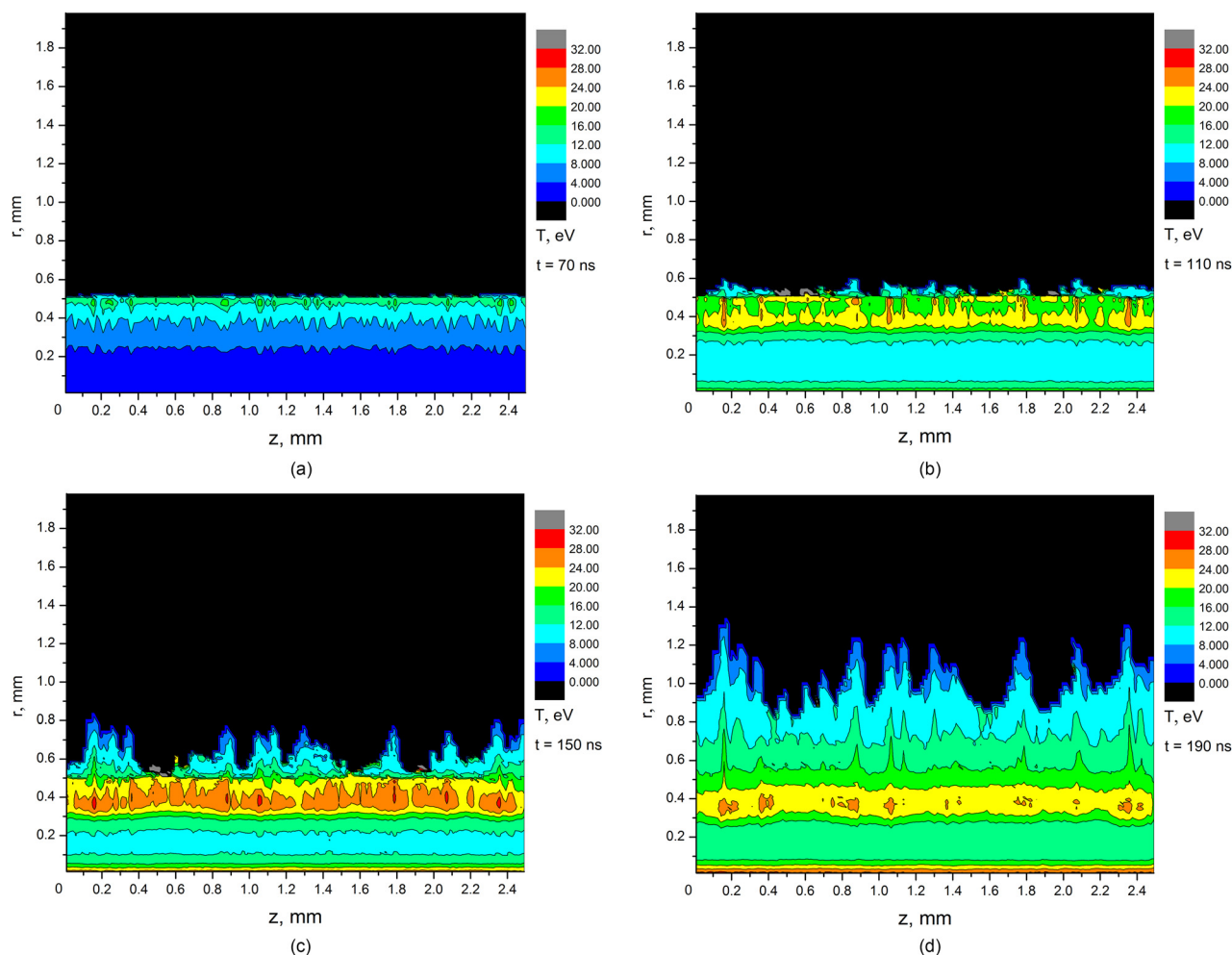


FIG. 4. Spatial temperature distributions at the times corresponding to the HSFC Pro camera images presented in Fig. 2: $t = 70$ (a), 110 (b), 150 (c), and 190 ns (d).

wires exploding in the mode of uniform current flow (in the absence of skin effect).^{51–56} It was shown^{26,27,53} that the most probable cause of the strata formation in exploding wires is thermal instability. A feature of the strata is their volumetric nature; that is, the instability develops throughout the volume occupied by the conductor, giving rise to alternating hot, low-density layers and relatively cold, dense material layers. As can be seen from Fig. 4, such a structure is not typical of the large-scale perturbations developing in the skin effect mode, and in this case, the instability is surface in nature. As shown below, the most probable cause of such a structure is the growth of flute instability,^{28,29,57,58} which is a type of Rayleigh–Taylor instability, that is, the instability of a heavy liquid situated above a light one in a gravitational field. In the case under consideration, the plasma acts as a heavy liquid, the magnetic field as light liquid, and the curvature of the magnetic force lines as gravity.^{29,57} In a nonuniform magnetic field, the plasma is subject to a force directed opposite to the magnetic field gradient, which expulses the plasma into the region of weak field. Therefore, flute instability is inherent in magnetic configurations in which the magnetic field lines are curved not into the interior, but toward the exterior of the confined plasma, as in our case. The development of flute instability is accompanied by the ejection of plasma across the magnetic field as "tongues" extending along the magnetic field lines. The growth rate of the instability can be estimated as^{58,59}

$$\gamma_{fl} \approx \frac{v_{Ti}}{\sqrt{R\chi}}, \quad (8)$$

where $v_{Ti} \sim \sqrt{\frac{T}{m_i}}$ is the thermal velocity of the plasma ions, m_i is the ion mass, R is the radius of curvature of the magnetic field lines, and $\chi = \left(\frac{1}{\rho} \frac{\partial \rho}{\partial r}\right)^{-1}$. In our case, R and χ are approximately equal to the conductor radius, and the instability growth rate can be estimated as $\gamma_{fl} \approx 10^{-7} \text{ s}^{-1}$; that is, the time of growth of flute instability should be of the order of 100 ns, as observed in experiments and predicted by numerical simulations.

It should be noted that the flute instability theories^{28,29,57–59} have been developed for idealized systems. They, first, assume the existence of a stationary (possibly unstable) state in which the plasma thermal pressure is balanced by the magnetic field pressure and, second, disregard dissipative processes such as magnetic field diffusion and plasma Joule heating. However, even these simplified theories do not allow exact analytical solutions. For instance, relation (8) gives an estimate of the flute instability increment in the long-wave limit.⁵⁹ In our case, however, dissipative processes play a leading part, and the plasma pressure is substantially greater than the magnetic field pressure due to shock-wave processes and Joule heat release. For all that, in our case, too, relation (8) allows a reasonable estimate of the time of growth of the large-scale instabilities observed both in experiments and in simulations.

As noted in Ref. 29, flute instability can be induced by electric currents, and the magnetic field energy or the plasma thermal energy can serve as an energy reservoir for the

growth of the instability. In the latter case, the buildup of perturbations is due to the nonuniformity of the plasma pressure.²⁹ This mechanism is probably realized in our case. This is testified by the time behavior of different types of energy in the conductor shown in Fig. 3. As can be seen in the figure, the kinetic energy of the conductor material is close to zero, and the thermal energy increases due to Joule energy input within about 150 ns. Thereafter, the growing plasma "tongues" increase the kinetic energy, whereas the thermal energy stops increasing (see Fig. 3), despite the continuing Joule heat release. Thus, the thermal energy of the plasma is converted into kinetic energy due to the nonuniformity of the plasma pressure. As the plasma tongues grow, the magnetic energy concentrated in the conductor material increases due to the increase in the volume occupied by the plasma. As the low-density and relatively cold tongue plasma has a low conductivity, it transfers only a small portion (a few percent) of the generator current.

To demonstrate that the curvature of the magnetic field lines is crucial in the development of large-scale instabilities, we have simulated the explosion of a conductor for a planar case. The simulation was performed in the (x, z) geometry symmetric about the z -axis with the magnetic field directed along the y -axis. The initial conditions were the same as those described in Section III. The boundary conditions for the y component of the magnetic field vector were the following: $B_y = 0$ at $x = 0$; $B_y = 2I(t)/(cr_0)$ at $x = X_{\max}$, where $I(t)$ is the current flowing through the conductor (its waveform was taken the same as for the cylindrical case), $r_0 = 0.5 \text{ mm}$ is the initial radius of the cylindrical conductor in the experiments performed on the MIG system, and X_{\max} is the maximum x coordinate of the Eulerian grid. The simulation results are presented in Figs. 3 and 5. Figure 3 shows the time behavior of the voltage across the load (curve δ). It can be seen that the load voltage in the planar case is, on the average, about half that is obtained for the cylindrical case, and so does the energy deposited in the conductor. The latter is due to that in the planar case, in contrast to the cylindrical one, the shock wave propagating through the conductor does not cause cumulative effects. Figure 5 shows the spatial temperature distribution in the conductor at $t = 190 \text{ ns}$. It can be

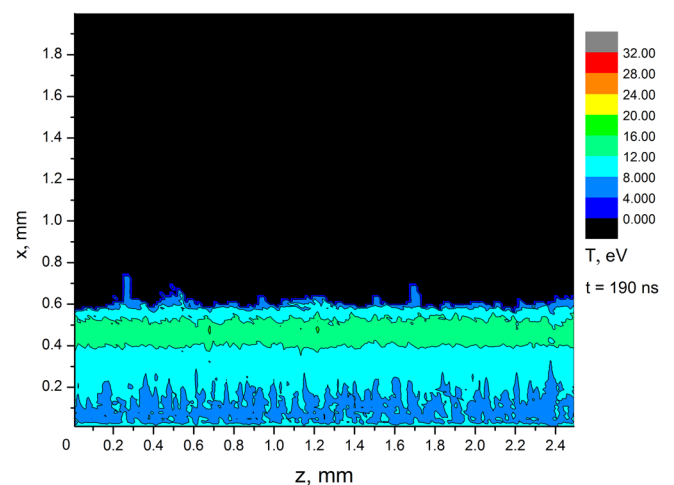


FIG. 5. Spatial temperature distribution for the planar case at $t = 190 \text{ ns}$.

seen that the temperature is distributed inhomogeneously in the conductor. It seems that the perturbations occurring inside the conductor at low temperatures are related to thermal instabilities, whereas the surface perturbations, though not as developed as in the cylindrical case (see Fig. 4(d)), are probably related to flute instabilities. Flute instabilities can develop at the boundary between a plasma and a magnetic field even if the magnetic field lines are not curved.²⁹ In this situation, the necessary condition for the instabilities to develop is the presence of a force directed from the plasma toward its confining magnetic field. In the case under consideration, this force is due to the excess of the plasma thermal pressure over the magnetic pressure induced by shock-wave heating and Joule heat release. In the cylindrical case, the pressure difference is even greater, about twice as that in the planar case. However, as can be seen by comparing Figs. 4(d) and 5, the difference in perturbation amplitudes is very large, indicating that the curvature of the magnetic field lines is the governing factor in the development of large-scale instabilities.

Returns to the cylindrical case and discusses the issues related to the stability of nonlinear magnetic diffusion waves. As mentioned above, it was shown³⁰ that in an NMDW propagating in a conductor, the modes with wavelengths of the order of the conductor thickness are not subject to thermal instabilities. Whether the short-wave modes are stable can be elucidated only by means of MHD calculations.

The propagation of a nonlinear diffusion wave through a conductor is illustrated by Figs. 6–8. Figure 6 shows the radial distributions of the conductor thermodynamic parameters (temperature and density), conductivity, and current density averaged over the coordinate z . The data presented in Fig. 6(a) correspond to the time (the 10th ns) at which the field at the conductor surface had reached the value B_0 , and a nonlinear diffusion wave began to form. The fluctuations in the radial distribution of the conductivity are due to random variations of the material density, which were set at the beginning of the calculation. Figure 6(b) shows the parameters of the conductor during the propagation of the shock wave and the nonlinear magnetic diffusion wave (at the 50th ns). As can be seen from this figure, the position of the current density maximum approximately coincides with the position of the material density maximum; that is, in this case, the NMDW and the shock wave propagate with about the same velocity. Figure 6(c) shows the parameters of the conductor at the time (the 90th ns) at which the shock wave and the nonlinear diffusion wave arrive at the axis.

Figures 7 and 8 present two-dimensional distributions of the material density (Figs. 7(a) and 8(a)) and current density $j = \sqrt{j_z^2 + j_r^2}$ (Figs. 7(b) and 8(b)) at different times. The data shown in Figs. 7 (the 50th ns) and 8 (the 90th ns) refer, respectively, to the shock wave and the NMDW propagating through the conductor and to their arrival at the axis. Analyzing these figures, we can conclude that the NMDW

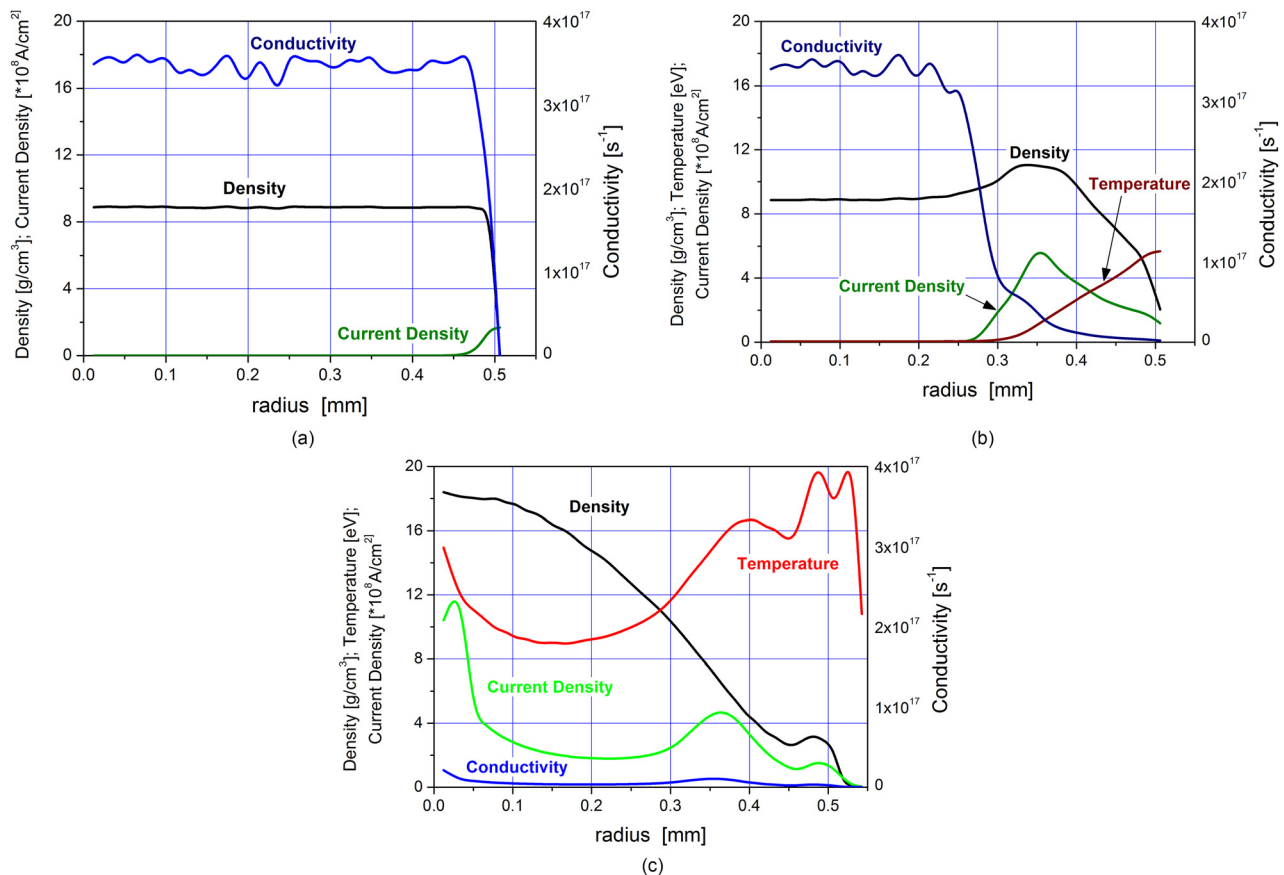


FIG. 6. Radial distributions of the conductor thermodynamic parameters (temperature and density), conductivity, and current density averaged over the z coordinate: $t = 10$ (a), 50 (b), and 90 ns (c).

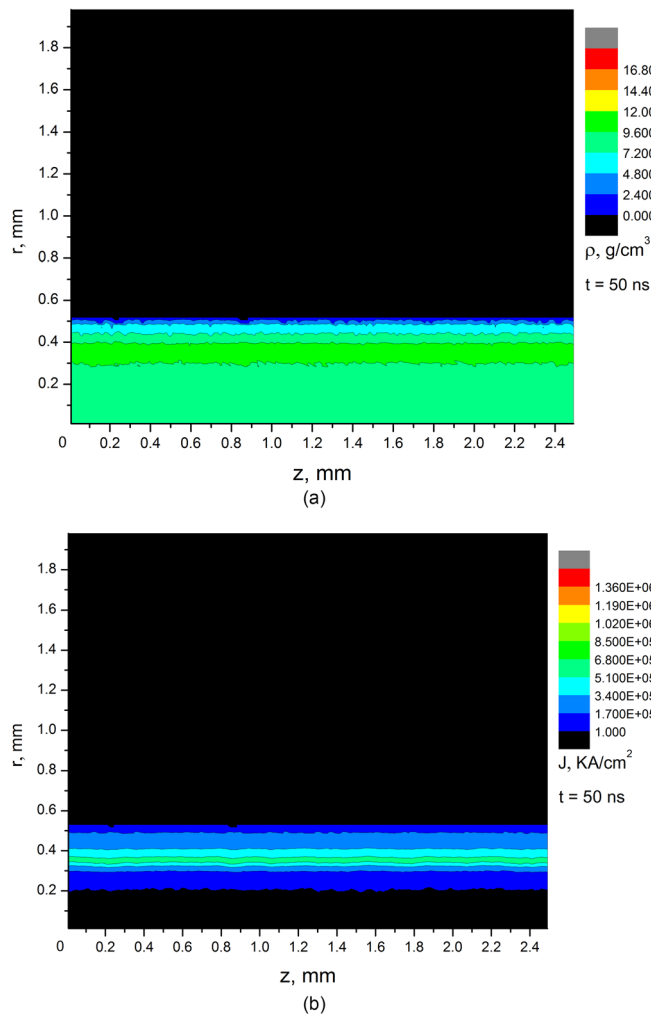


FIG. 7. Spatial distributions of the material density (a) and current density (b) during the propagation of an NMDW and a shock wave through a conductor ($t = 50$ ns).

front is not subject to thermal instabilities. The axial fluctuations of the current density that can be seen in Fig. 7(b) are due to the initially nonuniform distribution of the metal conductivity, and their amplitude does not increase during the propagation of the NMDW. Therefore, we see a uniform current density distribution at the time of arrival of the NMDW at the axis (see Fig. 8(b)). At the same time, behind the NMDW front, there are perturbations growing with time. They are most pronounced near the conductor surface, in relatively low-density layers, and are probably the result of thermal instability. The growth rate of the thermal instability is proportional to the derivatives of the resistivity with respect to temperature, $\frac{\partial \delta}{\partial T}$, and density, $\frac{\partial \delta}{\partial \rho}$.²⁶ The derivative $\frac{\partial \delta}{\partial \rho}$ reaches maximum values at nearly critical densities,^{26,49,60} i.e., in low-density layers. The growing thermal instability causes nonuniformity in the pressure at the plasma surface. This, in turn, gives rise to flute instability. The flute instability wavelength is determined by the scale of the pressure nonuniformity, i.e., by the thermal instability wavelength (see Figs. 6 and 8). The latter, in turn, is determined by the balance between the rates of the Joule heat release and heat removal by conduction.^{26,27}

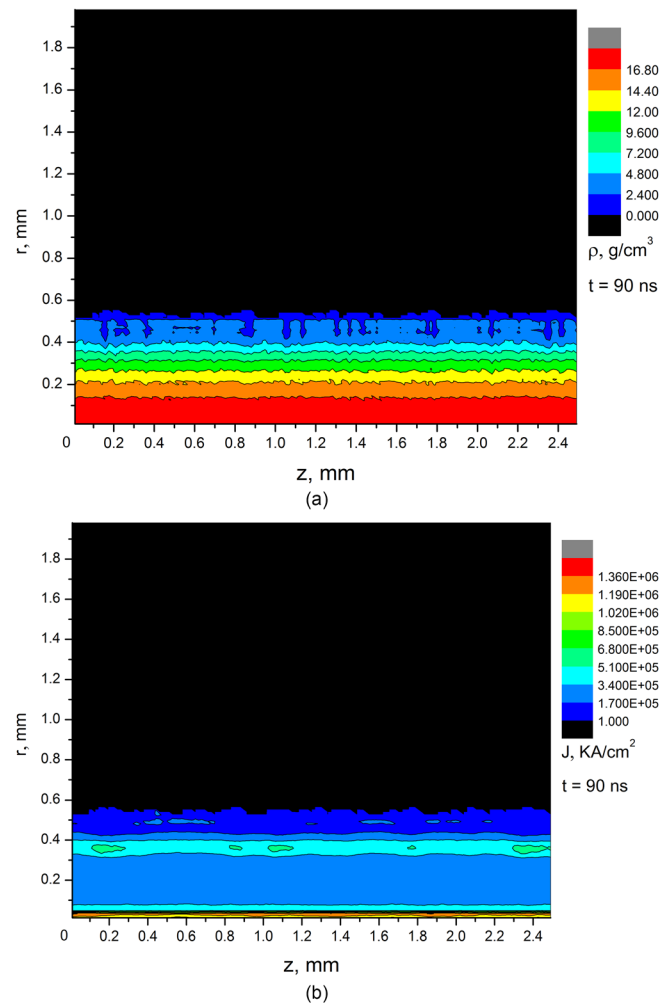


FIG. 8. Spatial distributions of the material density (a) and current density (b) during the propagation of an NMDW and a shock wave through a conductor ($t = 90$ ns).

V. CONCLUSION

Thus, the results of experiments with exploding copper conductors, performed on the MIG facility (providing currents of amplitude about 2.5 MA and rise time 100 ns), have been analyzed. With an HSFC Pro four-frame optical camera providing an exposure time of 3 ns, the large-scale instabilities of wavelength 0.2–0.5 mm were detected on the conductor surface. The instabilities show up as plasma "tongues" extended along the magnetic field lines and propagating with a velocity of $\sim 10^6$ cm/s in the opposite direction to the magnetic field gradient. Analysis was performed using a two-dimensional MHD code based on the particle-in-cell method that allowed a two-dimensional simulation of the explosion of conductors. It has been shown that the structures observed in the experiments were formed most probably due to flute instabilities. The growth of flute instabilities is predetermined by the development of thermal instabilities near the conductor surface. Instabilities of this type arise behind the front of a nonlinear magnetic diffusion wave propagating through a conductor. The wavefront, however, is not subject to thermal instabilities.

ACKNOWLEDGMENTS

The work was supported in part by the Russian Science Foundation, Grant No. 16-19-10142.

- ¹S. Slutz, C. Olson, and P. Peterson, *Phys. Plasmas* **10**(2), 429–437 (2003).
- ²E. Azizov, S. Alikhanov, E. Velikhov, M. Galanin, V. Glukhikh, E. Grabovsky, A. Gribov, G. Dolgachev, A. Jitlukhin, and J. G. Kalinin, *Plasma Devices Oper.* **12**(2), 123–132 (2004).
- ³W. A. Stygar, M. Cuneo, D. Headley, H. Ives, R. Leeper, M. Mazarakis, C. Olson, J. Porter, T. Wagoner, and J. Woodworth, *Phys. Rev. Spec. Top. - Accel. Beams* **10**(3), 030401 (2007).
- ⁴W. Stygar, T. Awe, J. Bailey, N. Bennett, E. Breden, E. Campbell, R. Clark, R. Cooper, M. Cuneo, and J. Ennis, *Phys. Rev. Spec. Top. - Accel. Beams* **18**(11), 110401 (2015).
- ⁵A. A. Kim, M. Mazarakis, V. Sinebryukhov, B. M. Kovalchuk, V. Visir, S. Volkov, F. Bayol, A. N. Batrikov, V. Durakov, and S. Frolov, *Phys. Rev. Spec. Top. - Accel. Beams* **12**(5), 050402 (2009).
- ⁶V. Aleksandrov, V. Gasilov, E. Grabovski, A. Gritsuk, Y. N. Laukhin, K. Mitrofanov, G. Oleinik, O. Ol'khovskaya, P. Sasorov, and V. Smirnov, *Plasma Phys. Rep.* **40**(12), 939–954 (2014).
- ⁷T. W. Sanford, R. E. Olson, R. C. Mock, G. A. Chandler, R. J. Leeper, T. J. Nash, L. E. Ruggles, W. W. Simpson, K. W. Struve, and D. Peterson, *Phys. Plasmas* **7**(11), 4669–4682 (2000).
- ⁸V. Smirnov, S. Zakharov, and E. V. Grabovskii, *J. Exp. Theor. Phys. Lett.* **81**(9), 442–447 (2005).
- ⁹V. Mokhov, O. Burenkov, A. Buyko, S. Garanin, S. Kuznetsov, V. Mamyshev, A. Startsev, and V. Yakubov, *Fusion Eng. Des.* **70**(1), 35–43 (2004).
- ¹⁰I. R. Lindemuth, *Phys. Plasmas* **22**(12), 122712 (2015).
- ¹¹S. Slutz, M. Herrmann, R. Vesey, A. Sefkow, D. Sinars, D. Rovang, K. Peterson, and M. Cuneo, *Phys. Plasmas* **17**(5), 056303 (2010).
- ¹²M. R. Gomez, S. A. Slutz, A. B. Sefkow, D. B. Sinars, K. D. Hahn, S. B. Hansen, E. C. Harding, P. F. Knapp, P. F. Schmit, and C. A. Jennings, *Phys. Rev. Lett.* **113**(15), 155003 (2014).
- ¹³C. Fowler, W. Garn, and R. Caird, *J. Appl. Phys.* **31**(3), 588–594 (1960).
- ¹⁴A. D. Sakharov, *Phys. - Usp.* **9**(2), 294–299 (1966).
- ¹⁵H. Knoepfel, *Pulsed High Magnetic Fields* (North-Holland, Amsterdam, 1970).
- ¹⁶Y. N. Bocharov, S. Krivosheev, and G. Shneerson, *Pis' ma Zh. Tekh. Fiz.* **8**(4), 212–216 (1982).
- ¹⁷S. Krivosheev, V. Titkov, and G. Shneerson, *Tech. Phys.* **42**(4), 352–366 (1997).
- ¹⁸R. Kinslow, *High-Velocity Impact Phenomena* (Academic Press, New York, 1970).
- ¹⁹S. Rashleigh and R. Marshall, *J. Appl. Phys.* **49**(4), 2540–2542 (1978).
- ²⁰V. E. e. Fortov, *Phys. - Usp.* **50**(4), 333–353 (2007).
- ²¹T. Nash, C. Deeney, G. Chandler, D. Sinars, M. Cuneo, E. Waisman, W. Stygar, D. Wenger, S. Speas, and R. Leeper, *Phys. Plasmas* **11**(10), L65–L68 (2004).
- ²²M. D. Knudson, R. Lemke, D. Hayes, C. A. Hall, C. Deeney, and J. Asay, *J. Appl. Phys.* **94**(7), 4420–4431 (2003).
- ²³R. Lemke, M. Knudson, C. Hall, T. Haill, P. Desjarlais, J. Asay, and T. Mehlhorn, *Phys. Plasmas* **10**(4), 1092–1099 (2003).
- ²⁴G. Shneerson, *Sov. Phys. Tech. Phys.* **18**, 419 (1973).
- ²⁵A. Valuev, I. I. Dikhter, and V. Zeigarnik, *Zh. Tekh. Fiz.* **48**, 2088–2096 (1978).
- ²⁶V. I. Oreshkin, *Phys. Plasmas* **15**(9), 092103 (2008).
- ²⁷V. I. Oreshkin, *Tech. Phys. Lett.* **35**(1), 36–39 (2009).
- ²⁸B. Kadomtsev, *Collective Phenomena in Plasma* (Nauka, Moscow, 1976) [in Russian].
- ²⁹B. Kadomtsev, *Reviews of Plasma Physics* (Consultants Bureau, New York, 1980).
- ³⁰V. I. Oreshkin and S. Chaikovsky, *Phys. Plasmas* **19**(2), 022706 (2012).
- ³¹S. Chaikovsky, V. I. Oreshkin, I. Datsko, N. Labetskaya, and N. A. Ratakhin, *Phys. Plasmas* **21**(4), 042706 (2014).
- ³²S. Chaikovsky, V. I. Oreshkin, I. Datsko, N. Labetskaya, D. Rybka, and N. A. Ratakhin, *Phys. Plasmas* **22**(11), 112704 (2015).
- ³³K. J. Peterson, T. J. Awe, P. Y. Edmund, D. B. Sinars, E. S. Field, M. E. Cuneo, M. C. Herrmann, M. Savage, D. Schroen, and K. Tomlinson, *Phys. Rev. Lett.* **112**(13), 135002 (2014).
- ³⁴A. Velikovich and P. Schmit, *Phys. Plasmas* **22**(12), 122711 (2015).
- ³⁵A. V. Luchinsky, N. A. Ratakhin, V. F. Feduschak, and A. N. Shepelev, *Izv. Vyssh. Uchebn. Zaved. Fiz.* **40**, 67 (1997).
- ³⁶V. Petin, S. Shljakhtun, V. I. Oreshkin, and N. A. Ratakhin, *Tech. Phys.* **53**(6), 776–782 (2008).
- ³⁷S. Chaikovsky, V. I. Oreshkin, G. Mesyats, N. A. Ratakhin, I. Datsko, and B. Kablambaev, *Phys. Plasmas* **16**(4), 042701 (2009).
- ³⁸S. Chaikovsky, A. Chuvatin, and V. I. Oreshkin, *Instrum. Exp. Tech.* **55**(2), 209–217 (2012).
- ³⁹Y. L. Bakshaev, A. Bartov, P. Blinov, A. Chernenko, S. Dan'ko, Y. G. Kalinin, A. Kingsep, V. Korolev, V. Mizhiritskiĭ, and V. Smirnov, *Plasma Phys. Rep.* **33**(4), 259–270 (2007).
- ⁴⁰T. Awe, B. Bauer, S. Fuelling, I. Lindemuth, and R. Siemon, *Phys. Plasmas* **17**(10), 102507 (2010).
- ⁴¹K. J. Peterson, D. B. Sinars, P. Y. Edmund, M. C. Herrmann, M. E. Cuneo, S. A. Slutz, I. C. Smith, B. W. Atherton, M. D. Knudson, and C. Nakhleh, *Phys. Plasmas* **19**(9), 092701 (2012).
- ⁴²K. J. Peterson, P. Y. Edmund, D. B. Sinars, M. E. Cuneo, S. A. Slutz, J. M. Koning, M. M. Marinak, C. Nakhleh, and M. C. Herrmann, *Phys. Plasmas* **20**(5), 056305 (2013).
- ⁴³T. J. Awe, K. J. Peterson, E. P. Yu, R. D. McBride, D. B. Sinars, M. R. Gomez, C. A. Jennings, M. R. Martin, S. E. Rosenthal, and D. Schroen, *Phys. Rev. Lett.* **116**(6), 065001 (2016).
- ⁴⁴V. I. Oreshkin, R. Baksht, N. A. Ratakhin, A. V. Shishlov, K. Khishchenko, P. Levashov, and I. Beilis, *Phys. Plasmas* **11**(10), 4771–4776 (2004).
- ⁴⁵V. Oreshkin, K. V. Khishchenko, P. R. Levashov, A. Rousskikh, and S. Chaikovskii, *High Temp.* **50**(5), 584–595 (2012).
- ⁴⁶S. Kolgatin and A. Khachatur'yants, *Teplotiz. Vys. Temp.* **20**(3), 447–451 (1982).
- ⁴⁷I. D. Bakulin, V. Kuropatenko, and A. Luchinskii, *Zh. Tekh. Fiz.* **46**, 1963–1969 (1976).
- ⁴⁸V. I. Oreshkin, R. Baksht, A. Y. Labetsky, A. Rousskikh, A. V. Shishlov, P. Levashov, K. Khishchenko, and I. Glazyrin, *Tech. Phys.* **49**(7), 843–848 (2004).
- ⁴⁹G. A. Mesyats, *Pulsed Power* (Springer Science & Business Media, 2007).
- ⁵⁰V. I. Oreshkin, S. Chaikovsky, N. A. Ratakhin, A. Grinenko, and Y. E. Krasik, *Phys. Plasmas* **14**(10), 102703 (2007).
- ⁵¹D. Sinars, T. Shelkovenko, S. Pikuz, M. Hu, V. Romanova, K. Chandler, J. Greenly, D. Hammer, and B. Kusse, *Phys. Plasmas* **7**(2), 429–432 (2000).
- ⁵²G. Sarkisov, P. Sasorov, K. Struve, and D. McDaniel, *J. Appl. Phys.* **96**(3), 1674–1686 (2004).
- ⁵³A. Rousskikh, V. I. Oreshkin, S. Chaikovsky, N. Labetskaya, A. V. Shishlov, I. Beilis, and R. Baksht, *Phys. Plasmas* **15**(10), 102706 (2008).
- ⁵⁴V. I. Oreshkin, A. Rousskikh, S. Chaikovsky, and E. Oreshkin, *Phys. Plasmas* **17**(7), 072703 (2010).
- ⁵⁵R. Baksht, S. Tkachenko, V. Romanova, A. Mingaleev, V. I. Oreshkin, A. Ter-Oganes'yan, T. Khattatov, T. Shelkovenko, and S. Pikuz, *Tech. Phys.* **58**(8), 1129–1137 (2013).
- ⁵⁶R. Baksht, A. Rousskikh, A. Zhigalin, V. I. Oreshkin, and A. Artyomov, *Phys. Plasmas* **22**(10), 103521 (2015).
- ⁵⁷N. Krall and A. Trivelpiece, *Principles of Plasma Physics* (McGraw-Hill Book Company, New York, 1973).
- ⁵⁸A. Ivanov, *Physics of Highly Nonequilibrium Plasmas* (Atomizdat, Moscow, 1977).
- ⁵⁹S. Ishimaru, *Basic Principles of Plasma Physics, Benjamin* (Benjamin, New York, 1973).
- ⁶⁰M. P. Desjarlais, *Contrib. Plasma Phys.* **41**(2–3), 267–270 (2001).